Extension of Methane Emission Rate Distribution for Permian Basin Oil and Gas Production Infrastructure by Aerial LiDAR

W. Minster Kunkel,* Asa E. Carre-Burritt, Grant S. Aivazian, Nicholas C. Snow, Jacob T. Harris, Tagert S. Mueller, Peter A. Roos, and Michael J. Thorpe*

Bridger Photonics, Inc., 2310 University Way Bldg 4-4, Bozeman, MT 59715, USA

E-mail: William.Kunkel@bridgerphotonics.com; Mike.Thorpe@bridgerphotonics.com

Abstract

Aerial LiDAR measurements of methane emissions at 7920 oil and gas production facilities in the Permian Basin yield an emission rate distribution extending to the detection sensitivity of the method, 2 kg/h at 90% probability of detection. The LiDAR measurements are analyzed in combination with the heavy tail portion (> 600 kg/h) of a distribution obtained from an intensive airborne solar infrared imaging spectrometry study by Cusworth et al. to yield a more complete emission rate distribution. Comparison of the data sets supports an assessment of the detection sensitivity of the solar infrared study at 300 kg/h at 50% probability of detection. Emissions detected by LiDAR increase the total emission rate for the survey region by a factor of 3.0 after controlling for scale factors such as survey area and number of scans per facility. Additionally, the role of spatial aggregation is highlighted as the cumulative emission rate distribution shifts toward larger source emission rates by a factor of three when detections are aggregated to facility size scales (150 m) rather than resolved to equipment size scales (2 m). The combined distribution derived for this study represents previously

underreported emission sources at rates below 300 kg/h resolved at equipment-level spatial precision.

Introduction

Methane is a potent greenhouse gas with a warming potential 80 times greater than that of CO_2 in a 20-year time frame.[1] Its current global emission rate is great enough to impact the climate significantly, with a greater contribution to global temperature rise in the first ten years after emission than CO_2 at its respective current emission rate.[2] Consequently, mitigation of methane emissions is viewed as particularly important for meeting climate goals within the next decade. Economic sectors including agriculture, waste disposal, and energy from oil and natural gas (O&G) are recognized as leading contributors to anthropogenic methane emissions, representing domains where emissions can be most meaningfully mitigated. In the O&G sector, emissions arise from discrete infrastructure elements and associated processes that can often be addressed with targeted intervention. Mitigation involves both the detection of emission sources and follow-up with repair and/or upgrade of emitting equipment. Identifying the most important emissions drivers and tracking the efficacy of mitigation efforts is key to making emissions reductions effective and efficient.[3,4]

Broadening the view of emissions from individual sources to a distribution of sources provides large-scale context to set meaningful mitigation goals. Past characterization of methane emission distributions has often relied on bottom-up models based on emission factors, such as those used for the U.S. Environmental Protection Agency's Greenhouse Gas Reporting Program and Greenhouse Gas Inventory. These models aim to identify dominant emission sources at the component or equipment levels but have been shown to misrepresent large-scale methane emissions distributions and the relative contribution of different elements,[3,5–8] with the greatest discrepancies existing in the production sector.[9] In addition, emissions factors are meant to apply nationally, whereas leakage rate distributions in

fact vary regionally and mitigation is performed locally.[7,8] To more precisely account for emissions, and to inform mitigation efforts, measurement campaigns have been conducted to obtain locally relevant empirical data within individual production basins throughout the United States and Canada.[10–15]

Many recent research efforts have focused on the Permian Basin because of its sizable share of U.S. O&G production, comprising 43% of domestic oil and 22% of natural gas produced annually.[16] Two studies on Permian methane emissions estimated region-wide O&G system leakage rates at 3.7% of production,[17,18] exceeding an estimated national average of 2.3%.[7] These studies leveraged satellite observations for inversion modeling and mass balance calculations, which are useful in benchmarking overall emissions but lack the detection sensitivity or spatial resolution needed to identify individual methane sources and understand their relation to infrastructure elements.

To provide a more specific account of emission sources, Cusworth et al. and Chen et al. each reported on measurement campaigns in the Permian Basin using aerially deployed solar infrared imaging spectrometers. The Cusworth study[19] covered 55,000 km^2 in the Midland and Delaware basins located in Texas and New Mexico. Emission sources were localized and attributed to individual facilities. Repeated sampling of the same sources was used to evaluate emission intermittency. Highly intermittent sources (0-25% persistence) were responsible for 48% of all point source emissions in the sample. The study by Chen et al.[20] was focused on the New Mexico Permian and encompassed over 90% of wellheads in that region. Chen compared the measured emission rate distribution from their study to that of Cusworth et al. in an overlapping spatial region and found that Cusworth detected progressively fewer emission sources at rates below roughly 300 kg/h, while their own study observed similarly reduced detections below 100-150 kg/h. Though the decline in detected emission sources suggests that the Cusworth data underrepresent the actual emission sources present below the roll-off rate, the heavy tail portion of the data set can still valuably inform models of the emission rate distribution.

For the present work, emissions in the Permian Basin were surveyed by Bridger Photonics' first generation Gas Mapping LiDAR (GML) sensor. A comparison of the fully detected part of the Cusworth emission rate distribution (> 600 kg/h) validates the assumption that the two surveys represent measurements from the same emission rate distribution, while the improved detection sensitivity of the GML survey is used to extend the measured distribution to significantly lower emission rates. Emission sources at rates underrepresented in the Cusworth survey are seen to contribute most of the total emission rate for the whole distribution.

Methods

Different technical specifications are offered by GML in comparison to high-altitude solar infrared imaging systems like the one used by Cusworth et al. Both technologies produce georegistered plume imagery that is used to locate the source of methane emissions and quantify their flow rate. Solar infrared systems can offer a greater capture rate (land area per time), particularly if flown at high altitude, whereas GML technology scans less area per time but offers improved spatial resolution and detection sensitivity. GML uses a spatially scanned laser spectroscopy technique to actively probe the optical absorption of methane plumes rather than passive imaging based on solar illumination. The instrument is flown at altitudes in the hundreds of meters rather than several km. GML's measured detection sensitivity is 0.41 kg/h per m/s wind speed at 90% probability of detection,[21] or 2 kg/h at the average wind speed of 4.9 m/s in Midland, TX.[22] Scans are performed at a flight altitude of 250 m with 1 m maximum distance between LiDAR measurement points. The GAO/AVIRIS-NG detection system used by Cusworth[19] has a 4-8 m ground pixel size at the flight altitudes used in the study (4.5 km and 8 km).

To compare spatial characteristics of the two detection systems, consider an example of plume imagery overlaid on satellite visible imagery shown in Fig. 1. The same facility

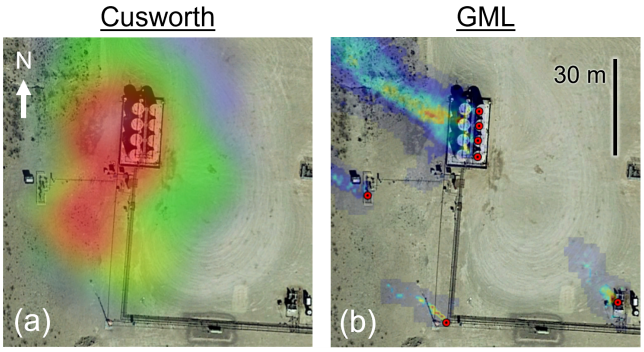

Figure 1: Example facility overlay with methane plume images from Cusworth (a) and GML (b) scans superimposed on satellite imagery (courtesy Google Earth). GML emission locations are marked by red dots. Cusworth and GML plumes were observed on different dates; the GML image comprises plumes observed on multiple dates. GML identifies unique emission sources at an interval of 4-5 m on a tank battery (upper center).

was observed by both AVIRIS-NG and GML on different dates. In (a), two possible gas concentration peaks are not quite distinguishable, whereas in (b), multiple GML plumes are visible. Pins mark localization of point sources with a precision of 2 m, which roughly corresponds to the size of typical production equipment.

Beyond using different technology and flight altitudes, the Cusworth and GML surveys differ in ways concerning time range, survey area, scan repetitions, and source aggregation. As detailed below, we perform checks to support the assumption that GML and Cusworth samples were drawn from the same emission rate distribution. We then describe the mathematical considerations needed for analysis.

Simple characteristics of the GML sample suggest similarity to Cusworth. First, 96.0% of GML detection locations lie within Cusworth's survey region (see GAO survey polygons in Ref. 19), with the remaining GML detections less than 70 km from the Cusworth survey boundaries. Second, the GML sample includes O&G production sites belonging to 28 operators, indicating a degree of operator diversity which is likely needed to represent the larger distribution. Third, changes in regional emissions driven by production volume can be broadly estimated using O&G production data. Average oil and gas production in Texas and New Mexico differed by less than 3% between the two survey times (Fig. S1), suggesting

little change in emissions from production scale. Finally, the Cusworth data have been filtered in this work to exclude detections from O&G pipelines and unclassified sources. GML data include detections from production facilities only. Excluding pipelines has a minimal effect on the Cusworth distribution, as mentioned in the analysis.

Perhaps more significantly, the GML survey covered fewer facilities than the Cusworth survey. Cusworth estimates that their survey area covered 72,000 wellheads, not counting other infrastructure, whereas GML covered 7920 facilities, which includes wells and other production infrastructure. Fewer scans were performed per site with GML (Fig. S2), with two as the median number of scans per site, whereas in Cusworth, the median number of scans is nine. Cusworth detections were filtered to those with $N \geq 3$ scans to select for higher accuracy in quantified persistence. GML sources detected in a first scan were often revisited in the following days to determine a binary measure of persistence. Since these repetitions are not independent, the GML scan count is effectively close to one for initial detection of emitters.

Before directly comparing the Cusworth and GML measurements to one another, the data must be reconciled to account for the different collection strategies of the two surveys. Differences arise mainly from temporal sampling styles and spatial aggregation. Reconciliation utilizes mathematical transformations to remap the Cusworth data by persistence and aggregate the GML data for comparison at the effective spatial resolution used by Cusworth. We divide the differences into four categories: (a) spatial aggregation, or defining an emission source to be the sum of all plumes within a geographic area, (b) time averaging, which influences the reported emission rate for a given source, (c) classifying a sample set as single-scan or being comprised of many scans, and (d) in the case of multiple scans, considering the effect of emitters absent from the observations due to intermittency.

(a) Spatial aggregation.

Grouping of individual emitters within a proximity threshold sets a spatial unit of interest for comparison between sources. An emission "source" in this paper means a set of plumes falling into a defined group or aggregation area, whereas "emitter" means a source smaller than the spatial detection resolution of the measurement system, inclusive of processing. Cusworth employs a 150 meter diameter aggregation area to define its sources at the size of a typical well pad. Since grouping individual emitters into the same source increases the represented emission rates via summation, GML detections were also aggregated to 150 meter diameter groups for comparison on an equal basis.

Spatial analysis of GML data is performed by first assigning an emission origin point, or "location," to each detected plume. Detections observed at different times are associated with the same location if they are co-located within 2 m. Emission locations were spatially aggregated by considering all locations within 150 m to belong to the same aggregated source.

GML detections can also be aggregated to "facilities" described by polygons enclosing site assets. Facility polygons represent the boundaries around actual groups of surface infrastructure usually defined by the facility pad footprint. Polygons can be provided by operators based on site data or generated from aerial photography, in which case the polygon is drawn either manually or by an artificial intelligence model. A polygon is defined for every facility on a GML flight path regardless of whether an emission is actually detected. Comparing the number of GML locations found in each facility to the number per 150 meter aggregation diameter shows a near correspondence between the two aggregation styles (Fig. S3), supporting the use of 150 meter aggregation to represent facility size scales. A smaller aggregation area (30 meters) displays a steeper roll-off in number of detection locations per source. The proportion of facilities with at least one detection was found to be 38.2% in the GML data set, much higher than the reported 1.48% rate for Cusworth's data set. This may be explained by differences in detection sensitivity described in the analysis.

(b) Time averaging.

Plumes detected asynchronously require considerations on uniqueness and averaging. Cusworth presents emissions as persistence-adjusted values q which are effectively time averaged. These are calculated as the mean of all non-zero measured emission rates $\bar{q}$ times the persistence f, which may be written

$$q = f\bar{q}, \tag{1}$$

where $f = M/N$ with M as the number of non-zero unique detections, N as the number of scans, and

$$\bar{q} = \frac{1}{M}\sum_{i=1}^{M} q_i, \tag{2}$$

where q_i is a non-zero unique emission rate measurement.

Depending on the application, it can be useful to plot functions of the emission rate versus either q or $\bar{q}$. Persistence-adjusted emission rate q is often the quantity of interest in large-scale inventories. However, q does not represent the actual emission rate observed at the time of measurement. Whereas q tends to conflate persistence with the observed emission rate, $\bar{q}$ is the average of measurements when the source is actually emitting. When sample sets with different temporal sampling modes are to be compared (e.g. "single-scan" or "repetitive," as described below), it becomes important to use $\bar{q}$.

For GML locations, the average emission rate $\bar{q}$ is calculated following Eq. 2 as the average of non-zero emission rates resulting from each scan. Scan measurements, in turn, may include multiple aerial passes and are calculated as an average of all emission rates (zero and non-zero) from all passes within a 12-hour time window. Separate time windows are treated as unique scans.

(c) Single scan vs. repetitive scanning

Temporal sampling influences the character of the measured sample. At the lowest sampling limit is a single scan, in which all potentially emitting sites are observed only once. Persis-

tence cannot be directly inferred from a single scan since individual sources are not observed in both emitting and non-emitting states. At the opposite sampling limit is a highly repetitive sample, in which all sources are observed so frequently that the persistence is known to arbitrary precision. The GML data set closely approximates single-scan sampling, whereas the Cusworth data set is moderately repetitive.

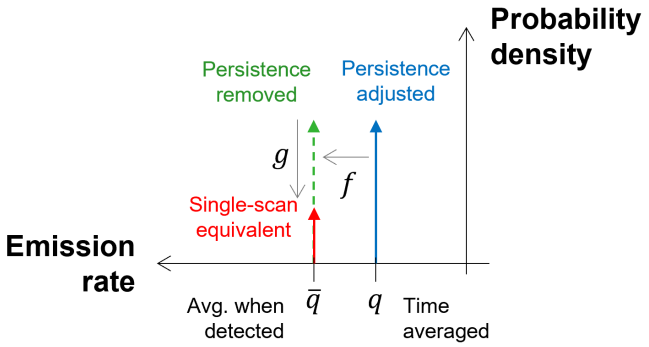

Figure 2: Transformation of a probability density function into different forms using the observed persistence f and modified persistence g. Emission rate increases to the left.

Transformation of the probability density function (PDF) can be used to compare distributions obtained in these different sampling styles. Recall that the PDF can be defined as the function of a random variable x over which integration yields the probability that x falls within the integration range. Consider a point on the PDF, which is represented as a delta function in Fig. 2. The persistence adjusted PDF (blue), where the emission rate is q, is accessible only from a repetitive sample set and not a single scan, since the persistence f is needed to obtain q. However, the PDF can be replotted at $\bar{q}$, which effectively removes the persistence from the emission rate. This represents the PDF at the average non-zero emission rate that was actually measured in the field. This shift produces an intermediate result with an effectively higher emission rate (green dashed). However, to obtain a correctly weighted PDF for integration (red), the probability of observing the source must be reduced by the persistence. The weight is written as g to represent a modified persistence discussed below. For a continuous PDF, the remapping of q to $\bar{q}$ and the persistence weighting g applies to all points on the curve.

With the above modifications, the new PDF originating from a repetitively sampled data set mimics the PDF obtained from a single scan. A single scan reports all measured emission rates at $\bar{q}$ and contains information about probability density through counts rather than through persistence. Assuming that the single-scan sample is sufficiently large, its PDF should match the remapped "single-scan equivalent" obtained from the repetitive sample. Related distributions, such as the cumulative distribution function (CDF) and cumulative emission rate function, are then also directly comparable, aside from possible scale factors. We utilize this to compare the GML and Cusworth data sets despite their different sampling styles. The transformation is demonstrated on the Cusworth cumulative emission rate distribution (Section S1).

(d) Selection bias

A more accurate single-scan equivalent PDF can be obtained from a repetitive data set using a modified persistence g. The modification is meant to compensate for missed emission sources arising from a limited number of scans. We begin by recognizing that the observed persistence $f = M/N$ is actually a conditional probability $P(A|B)$, where A is the event that an intermittent source was emitting during a given scan, and B is the event that the source was emitting at least once in N scans. Bayes' theorem can then be used to express the true persistence

$$P(A) = \frac{P(B)P(A|B)}{P(B|A)}. \tag{3}$$

Using the shorthand $g \equiv P(A)$ and substituting $P(A|B) = f$, $P(B|A) = 1$, and $P(B) = 1 - (1-g)^N$ from the binomial probability mass function yields

$$f = \frac{g}{1-(1-g)^N}, \tag{4}$$

which is plotted in Fig. 3. The observed persistence departs from true persistence at low values by an amount that diminishes with increasing number of scans. The difference is

largest for sources with small-valued persistence. Since the observed persistence can take only M discrete values, we use a stepwise approximation to the curves. Taking for example $N = 3$, steps are placed at the allowed values of f, with transitions placed to intersect the curve halfway through each jump. We then approximate the persistence at each quantized value by the midpoint of each step. This maps the input values of f to output values g, as indicated by the dotted arrows. The resulting "true" persistence values g are strictly lower than the observed persistence f. This expresses the notion that the persistence should be corrected by the missed emitters that are not otherwise represented in the data set. For a nearly single-scan distribution such as GML, $g = 1$ is a suitable assumption because the observed sources have presumably self-selected into the sample at a rate proportional to the true persistence and frequency of occurrence.

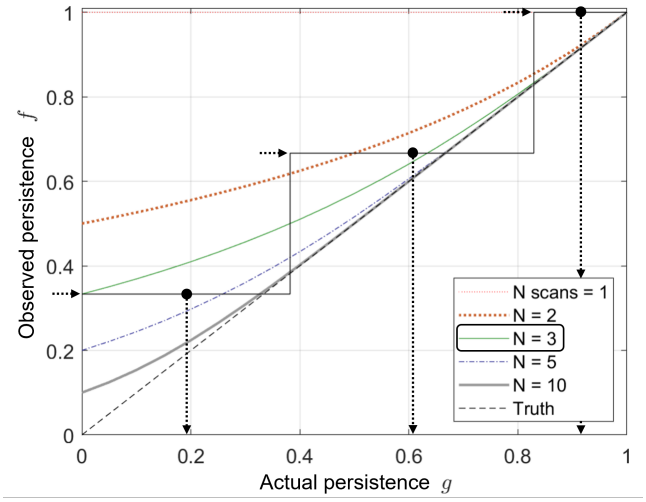

Figure 3: Persistence transformation to compensate selection bias. Stepwise function shows an example at $N = 3$ scans to demonstrate measurement quantization at $f = (1/3, 2/3, 1)$.

Results and discussion

With the above adaptations, we may now compare a repetitive, spatially aggregated data set such as Cusworth with an effectively single-scan, single-emitter data set such as GML. In this section, we will join the two data sets and model the underlying emission rate distribution.

Comparing the PDFs will validate the assumption that GML and Cusworth data represent the same distribution and quantify the detection sensitivity of the Cusworth survey. After considering 150 m spatially aggregated sources, we repeat the analysis on single-emission locations to demonstrate that spatial aggregation significantly increases the reported emission rates for a given distribution.

Distribution of spatially aggregated sources (150 m)

To join the data sets and model the shared emission rate distribution, we compare and fit the data sets using the cumulative distribution function (CDF). The CDF allows for differences in sample scale and variability, which is useful because of GML's smaller sample size. The discrete CDF for a single-scan equivalent distribution is given by

$$c(x) = \frac{\sum_{\bar{q} \geq x}^{\infty} g(\bar{q})}{\sum_{\bar{q}=x_L}^{\infty} g(\bar{q})}, \tag{5}$$

where x is the emission rate and $x \geq x_L$, with x_L as the lower bound of a range of interest. For clarity, the sum will be represented as a stepwise function. For Cusworth, g is given by the abovementioned approximation to Eq. 4, whereas for GML, $g = 1$. The lower bound x_L specifies the endpoint of the summation. For comparing two sets of detections, x_L is set to the greater of the two so-called full detection limits, below which the probability of detection for a nominal emitter becomes appreciably less than unity. We choose $x_L = 600$ kg/h as the effective full detection limit of Cusworth's measurements.

Single-scan equivalent CDFs are plotted in Fig. 4. The samples are seen to agree closely, with the maximum absolute residual indicated by the Kolmogorov-Smirnov (K-S) statistic.[23] The p-value corresponding to the K-S statistic is 0.831, meaning that if hypothetically both samples of this size were obtained from the same distribution, then 16.9% of all possible sample sets would have a smaller maximum residual than the value indicated. The number

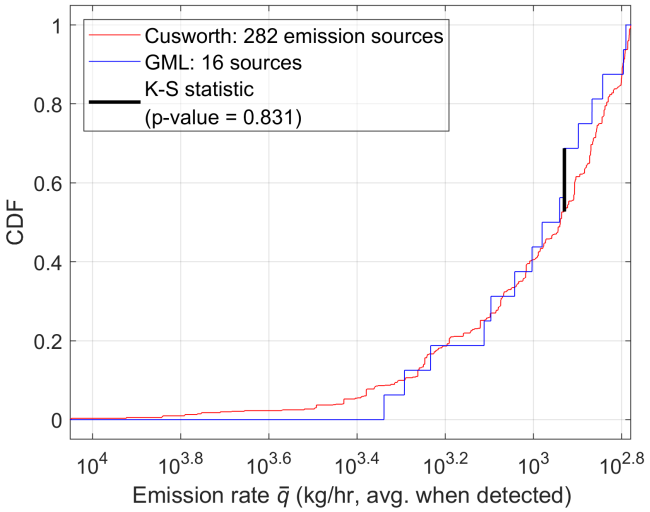

Figure 4: Cumulative distribution function (CDF) of single-scan equivalent Cusworth and GML data sets for emission rates above 600 kg/h. Kolmogorov-Smirnov (K-S) statistic and associated p-value are indicated.

of emission sources bears strongly on the expected sample variation. GML observed only 16 sources in the range of interest, whereas Cusworth observed 282. Though the K-S p-value does not affirmatively support the common identity of two sample distributions, it is capable of highlighting sample variations that would be statistically unlikely if the two samples were drawn from the same distribution. It also provides a convenient metric for goodness of fit, which will be used in later optimization steps. Relative to Cusworth, the GML sample somewhat underrepresents emitters above 2000 kg/h. These emitters represent a small part of the population, but since they have an outsize importance on the total emission rate, sampling variations can lead to noticeable deviations in the cumulative emission rate.

We next create a model of the distribution that represents both data sets. The model PDF follows a lognormal form,

$$p(x) \propto \exp\left[-b(x - x_0)^2\right], \tag{6}$$

where x is the base-10 logarithm of the emission rate. Integration over the range $x_L \leq x < \infty$

yields the CDF

$$c(x) = \frac{\text{erf}\left[\sqrt{b}(x - x_0)\right] - 1}{\text{erf}\left[\sqrt{b}(x_L - x_0)\right] - 1}, \tag{7}$$

which has been normalized to the integration range. The model contains two fit parameters, b and x_0, the values of which are optimized by a joint fitting process. A third parameter, h, is also introduced to allow for sample variation between the two data sets in the comparison range $x \geq x_L$. The three parameters are jointly optimized using a metric that involves p-values from three K-S comparisons: the model to GML scaled by h (p-value: p_1), the model to Cusworth (p_2), and Cusworth to scaled GML (p_3). Optimization minimizes the metric $1 - (p_1 p_2 p_3)^{1/3}$ to find the best-fit parameter values. The product $m = p_1 p_2 p_3$ represents the joint probability of all three K-S statistics occurring simultaneously, assuming each is an independent event. Since the events are not entirely independent, m is likely to somewhat underestimate the actual joint probability. This is neglected with the understanding that m is an approximation to the total probability of the fit. Outputs of the fitting process are detailed in Section S2. A nominal value of $x_L = 10$ kg/h is chosen to represent the full detection limit for GML. This value was chosen not to represent the detection sensitivity but to conservatively overestimate the detection limit for unit detection probability.

With the fit parameters obtained from the CDF, we now plot the PDF to compare the distributions across all emission rates. Results are shown in Fig. 5. Data are binned by emission rate and normalized in probability density to a reference number described on the vertical axis. The full detection limits of both data sets are shown by vertical dotted lines, with the region above Cusworth's limit shaded. Confidence bounds for the model are calculated to give the most extreme values of the PDF on the $m = 0.05$ contour of the parameter space. Error bars are placed at $\pm p_{\text{bin}}/\sqrt{n_{\text{bin}}}$, where p_{bin} is the value of the PDF for the bin and n_{bin} is the count of emission sources in the bin. All three traces (Cusworth, GML, and model) agree in the region above Cusworth's full detection limit. However, Cusworth's PDF diminishes rapidly at emission rates below the full detection limit. By comparing the

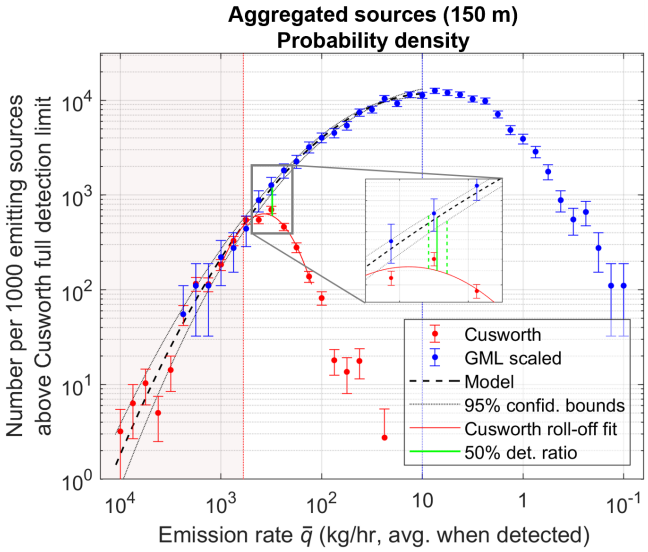

Figure 5: Scaled probability density functions of 150 m aggregated emission sources. Zoomed in view near the Cusworth sensitivity limit (inset) shows the 50% detection ratio with respect to model function and its confidence bounds.

lognormal model confidence bounds to Cusworth's data around the roll-off region, which is represented by an error-weighted cubic polynomial fit of the binned data, the 50% detection ratio is placed at 290-328 kg/h at 95% confidence. This emission rate is considerably higher than the detection limit quoted by Cusworth at 10-20 kg/h but is consistent with a previous estimate in the range 100-300 kg/h.[20] Interestingly, Cusworth's mean observed persistence versus emission rate also drops off rapidly beyond the 50% detection limit (Fig. S4), which would be consistent with reduced probability of detection from limited detection sensitivity. Without compensation, reduced detection probability leads to a significant underrepresentation of smaller emission sources. Comparing the PDFs at 100 kg/h, for example, shows that emission sources at this rate are in fact 50 times more common than the Cusworth measurements would suggest.

Equipment-scale emission rate distribution

To demonstrate the effect of spatial aggregation on the emission rate distribution, we now consider the distribution for equipment-scale emission sources. Performing the same model

fitting and analysis process as above shows the relationship between equipment-scale sources as measured by GML and spatially aggregated facility-scale emission sources as reported by Cusworth. Aggregation can be expected to transform and shift the distribution toward larger emission rates since co-located emitters count toward the same emission source. We aim to quantify this shift and point out its implications for emission rate thresholds representing a given fraction of the total emission rate.

In the following analysis, GML sources are considered in their native equipment-scale resolution and not aggregated to 150 m. Cusworth sources are not reported at finer resolution. Instead, we manually filter them based on associated plume imagery[24] to include only sources with a single point emission. Human analysts classified Cusworth plume images as either "single emitter" or "multiple or unclear." Detections classified as "single emitter" were selected for analysis, forming a subset of Cusworth's data that was applied to the same model fitting process as above. The data were cut to include only the first scan at each source, making the data set effectively single-scan. The filter to $N \geq 3$ scans was also removed and g set to unity. By changing the data selection to match GML's conditions, the number of Cusworth sources changed from 923 sources at 150 m to 645 single emitters. For GML, skipping aggregation increased the number of GML sources from 2935 to 7959, though the number of GML sources above the Cusworth full detection limit (600 kg/h) shrank from sixteen to seven. Though the smaller sample size causes the confidence bounds to widen, the comparison statistics do not oppose joining the two data sets. CDFs and residuals from the fitting process display similar behavior to 150 m sources (Fig. S5). Spatial aggregation significantly affects the Cusworth distribution; O&G pipeline sources do not do so (Section S3).

Single-emitter PDFs are shown together with aggregated source PDFs in Fig. 6. As expected, the probability density at lower emission rates is higher for single emitter sources than for aggregated sources. This is clearest in the range 10-100 kg/h, where the GML curves have significantly diverged as emission rates decrease. At 10 kg/h, single-emitter sources are observed six times more frequently than aggregated ones. The filters used to resample the

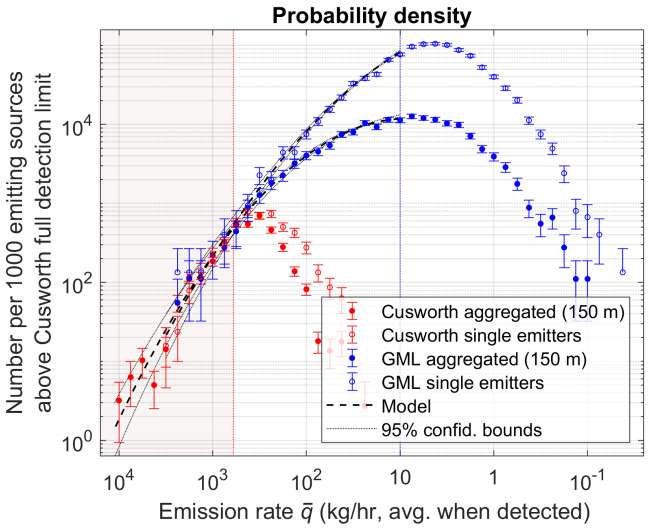

Figure 6: Probability density functions of emission sources aggregated at 150 m diameter and single emission sources. The single emitter trace has been scaled by the ratio of detected Cusworth sources, so the vertical axis refers to 1000 Cusworth sources at 150 m aggregation.

Cusworth data set do not appear to distort the distribution appreciably in comparison to the equivalent GML distribution. The two aggregation levels remain overlapped for emission rates over the Cusworth full detection limit, and the 50% detection ratio remains near 300 kg/h for single emitters (Fig. S6).

The resulting emissions can be numerically integrated to yield the cumulative emission rate distributions shown in Fig. 7. The exact sum is given by Eq. S1 (single-scan equivalent). The aggregated distributions overlap well for heavy tail emission rates larger than Cusworth's full detection limit. At smaller emission rates, the GML cumulative rate distribution continues to grow until reaching a plateau below 10 kg/h.

Expected error due to sample variation is shown in the plot. Error bounds show the 16 and 84 percentiles of the expected sample variation for an equivalently sized data set with the same number of detections above the corresponding full detection limit. These are found by running a Monte Carlo simulation of random sets of detections drawn from the model PDF. Sample error from rates below the corresponding full detection limit is neglected, as is instrument quantification error.

Since very large sources are slightly underrepresented in the GML data set due to sample

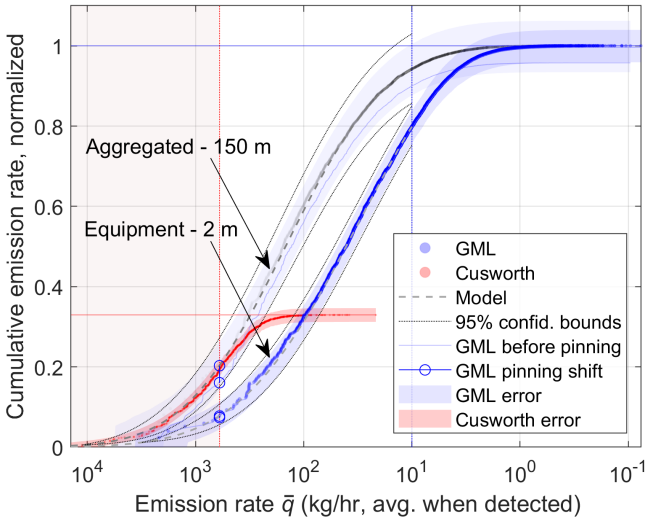

Figure 7: Cumulative emission rate distribution of 150 m aggregated emission sources (GML and Cusworth) and equipment-scale sources (GML only). Error bounds (shaded regions) describe predicted sample variation.

variation (see >2000 kg/h in Fig. 4), the GML curve has been vertically shifted by 0.039 in normalized units to pin its value to the model function at the Cusworth full detection limit. The pinning shift is within the sample error bounds, suggesting that the correction is within the likeliest range of magnitudes.

As shown by the top of the cumulative emission curves, the total emission rate of the scaled distribution of GML measurements is 3.0 times greater than measured by Cusworth. The difference is caused by false negative detections in the Cusworth study from emissions below the detection sensitivity (300 kg/h). While Cusworth's data would suggest that 90% of the total emission rate is contributed by 150-m aggregated sources larger than 264 kg/h, GML data suggest that the 90% threshold is 17 kg/h. When using equipment-scale resolution rather than facility aggregation, rate thresholds shrink significantly further. Relative to the 150 m aggregated curve, the equipment-level single emitters curve is horizontally shifted toward smaller emission rates by roughly a factor of three. From the shifted curve, GML data suggest that the threshold at 90% of total emissions for equipment is 5.4 kg/h (or using the estimated sample error from the plot, 3.8 to 7.1 kg/h). Since mitigation strategies are often based on identifying equipment for repair, it is important to consider the distribution

at this spatial resolution.

Although 5.4 kg/h is below the GML full detection limit conservatively selected for fitting (10 kg/h), it is above the measured detection sensitivity of 2 kg/h at 90% probability of detection. The shift to different emission rates depending on aggregation means that the detection sensitivity of a given system should be specified with a spatial source resolution when targeting a cumulative fraction of total emissions.

In summary, we have used GML survey data to extend the measured emission rate distribution for Permian Basin production infrastructure beyond Cusworth's sensitivity limits by roughly two orders of magnitude. GML detection data are scaled and supported by the larger and repetitively-scanned Cusworth data set. From the combined distribution, it is seen that emission sources with rates below the Cusworth detection sensitivity of 300 kg/h (at 50% probability of detection) contribute two thirds of the total emission rate observed in the survey region when measured at Gen. 1 GML sensitivity. Further, spatial aggregation of emission sources to the facility level shifts the cumulative emission rate distribution significantly toward larger rates. This paper has demonstrated that the total O&G production emission rate in the survey region is significantly greater than previously reported, with 90% of the total rate contributed from equipment-sized sources at emission rates above 5.4 kg/h. Continued measurements and analysis, complete with reconciliation between different emissions monitoring data sources, should inform actions to maximize the impact of mitigation efforts.

Acknowledgement

Bridger Photonics thanks the Advanced Research Program Agency – Energy (ARPA-E) MONITOR program and the Montana Board of Research and Commercialization Technology (MBRCT) for supporting the original development of GML hardware and analytics.

References

(1) Forster, P.; Storelvmo, T.; Armour, K.; Collins, W.; Dufresne, J.-L.; Frame, D.; Lunt, D. J.; Mauritsen, T.; Palmer, M. D.; Watanabe, M.; Wild, M.; Zhang, H. In *Climate Change 2021: The Physical Science Basis. Contribution of Working Group I to the Sixth Assessment Report of the Intergovernmental Panel on Climate Change*; Masson-Delmotte, V. et al. , Eds.; Cambridge University Press, 2021; Chapter The Earth's Energy Budget, Climate Feedbacks and Climate Sensitivity, pp 923–1054, see Table 7.15.

(2) Szopa, S.; Naik, V.; Adhikary, P.; Berntsen, T.; Collins, W. D.; Fuzzi, S.; Gallardo, A.; Kiendler-Scharr, Z.; Klimont, H.; Liao, N.; Under, N.; Zanis, P. In *Climate Change 2021: The Physical Science Basis. Contribution of Working Group I to the Sixth Assessment Report of the Intergovernmental Panel on Climate Change*; Masson-Delmotte, V. et al. , Eds.; Cambridge University Press, 2021; Chapter Short-lived Climate Forcers, pp 817–922, see Fig. 6.16.

(3) Brandt, A. R. et al. Methane leaks from North American natural gas systems. *Science* **2014**, *343*, 733–735.

(4) Allen, D. T. Methane emissions from natural gas production and use: Reconciling bottom-up and top-down measurements. *Current Opinion in Chemical Engineering* **2014**, *5*, 78–83.

(5) Zimmerle, D. J.; Williams, L. L.; Vaughn, T. L.; Quinn, C.; Subramanian, R.; Duggan, G. P.; Willson, B.; Opsomer, J. D.; Marchese, A. J.; Martinez, D. M.; Robinson, A. L. Methane Emissions from the Natural Gas Transmission and Storage System in the United States. *Environmental Science and Technology* **2015**, *49*, 9374–9383.

(6) Marchese, A. J.; Vaughn, T. L.; Zimmerle, D. J.; Martinez, D. M.; Williams, L. L.; Robinson, A. L.; Mitchell, A. L.; Subramanian, R.; Tkacik, D. S.; Roscioli, J. R.;

Herndon, S. C. Methane Emissions from United States Natural Gas Gathering and Processing. *Environmental Science and Technology* **2015**, *49*, 10718–10727.

(7) Alvarez, R. A. et al. Assessment of methane emissions from the U.S. oil and gas supply chain. *Science* **2018**, *361*, 186–188.

(8) Omara, M.; Zimmerman, N.; Sullivan, M. R.; Li, X.; Ellis, A.; Cesa, R.; Subramanian, R.; Presto, A. A.; Robinson, A. L. Methane Emissions from Natural Gas Production Sites in the United States: Data Synthesis and National Estimate. *Environmental Science and Technology* **2018**, *52*, 12915–12925.

(9) Rutherford, J. S.; Sherwin, E. D.; Ravikumar, A. P.; Heath, G. A.; Englander, J.; Cooley, D.; Lyon, D.; Omara, M.; Langfitt, Q.; Brandt, A. R. Closing the methane gap in US oil and natural gas production emissions inventories. *Nature Communications* **2021**, *12*, 4715.

(10) Duren, R.; Thorpe, A.; McCubbin, I. *The California Methane Survey*; 2020; California Energy Commission. Publication Number: CEC-500-2020-047.

(11) Harriss, R.; Alvarez, R. A.; Lyon, D.; Zavala-Araiza, D.; Nelson, D.; Hamburg, S. P. Using Multi-Scale Measurements to Improve Methane Emission Estimates from Oil and Gas Operations in the Barnett Shale Region, Texas. *Environmental Science and Technology* **2015**, *49*, 7524–7526.

(12) Vaughn, T. L.; Bell, C. S.; Pickering, C. K.; Schwietzke, S.; Heath, G. A.; Pétron, G.; Zimmerle, D. J.; Schnell, R. C.; Nummedal, D. Temporal variability largely explains top-down/bottom-up difference in methane emission estimates from a natural gas production region. *Proceedings of the National Academy of Sciences of the United States of America* **2018**, *115*, 11712–11717.

(13) Johnson, M.; Tyner, D.; McCole, E.; Conrad, B.; Milani, Z.; Seymour, S.; Roth, C.; Burtt, D.; Festa-Bianchet, S.; Mohammadikharkeshi, M.; Kirby, F.; Szekeres, A. Ap-

plication of Airborne LiDAR Measurements to Create Measurement-Based Methane Inventories in the Canadian Upstream Oil & Gas Sector. American Geophysical Union Fall Meeting 2021. 2021; pp GC24D–03.

(14) Peischl, J.; Eilerman, S. J.; Neuman, J. A.; Aikin, K. C.; de Gouw, J.; Gilman, J. B.; Herndon, S. C.; Nadkarni, R.; Trainer, M.; Warneke, C.; Ryerson, T. B. Quantifying Methane and Ethane Emissions to the Atmosphere From Central and Western U.S. Oil and Natural Gas Production Regions. *Journal of Geophysical Research: Atmospheres* **2018**, *123*, 7725–7740.

(15) Robertson, A. M.; Edie, R.; Field, R. A.; Lyon, D.; McVay, R.; Omara, M.; Zavala-Araiza, D.; Murphy, S. M. New Mexico Permian basin measured well pad methane emissions are a factor of 5-9 times higher than U.S. EPA estimates. *Environmental Science and Technology* **2020**, *54*, 13926–13934.

(16) Popova, O.; Long, G. *Advances in technology led to record new well productivity in the Permian Basin in 2021*; 2022; U.S. Energy Information Administration, https://www.eia.gov/todayinenergy/detail.php?id=54079.

(17) Schneising, O.; Buchwitz, M.; Reuter, M.; Vanselow, S.; Bovensmann, H.; Burrows, J. P. Remote sensing of methane leakage from natural gas and petroleum systems revisited. *Atmospheric Chemistry and Physics* **2020**, *20*, 9169–9182.

(18) Zhang, Y. et al. Quantifying methane emissions from the largest oil-producing basin in the United States from space. *Science Advances* **2020**, *6*, eaaz5120.

(19) Cusworth, D. H.; Duren, R. M.; Thorpe, A. K.; Olson-Duvall, W.; Heckler, J.; Chapman, J. W.; Eastwood, M. L.; Helmlinger, M. C.; Green, R. O.; Asner, G. P.; Dennison, P. E.; Miller, C. E. Intermittency of Large Methane Emitters in the Permian Basin. *Environmental Science and Technology Letters* **2021**, *8*, 567–573.

(20) Chen, Y.; Sherwin, E. D.; Berman, E. S. F.; Jones, B. B.; Gordon, M. P.; Wetherley, E. B.; Kort, E. A.; Brandt, A. R. Quantifying regional methane emissions in the New Mexico Permian Basin with a comprehensive aerial survey. *Environmental Science and Technology* **2022**, *56*, 4317–23.

(21) Bell, C.; Rutherford, J.; Brandt, A.; Sherwin, E.; Vaughn, T.; Zimmerle, D. Single-blind determination of methane detection limits and quantification accuracy using aircraft-based LiDAR. *Elementa: Science of the Anthropocene* **2022**, *10*, 00080.

(22) National Weather Service, Midland Texas Monthly Wind Averages. [Data set]. https://www.weather.gov/maf/cli_maf_winds (Retrieved 2022-Dec-12).

(23) Bartoszyński, R.; Niewiadomska-Bugaj, M. *Probability and Statistical Inference*; Wiley, 1996.

(24) Cusworth, D. Methane plumes for NASA/JPL/UArizona/ASU Sep-Nov 2019 Permian campaign. 2021; [Data set]. Zenodo. https://doi.org/10.5281/zenodo.5610307.

TOC Graphic

Supporting Information

Extension of Methane Emission Rate Distribution for Permian Basin Oil and Gas Production Infrastructure by Aerial LiDAR

W. Minster Kunkel,* Asa E. Carre-Burritt, Grant S. Aivazian, Nicholas C. Snow, Jacob T. Harris, Tagert S. Mueller, Peter A. Roos, and Michael J. Thorpe*

Bridger Photonics, Inc., 2310 University Way Bldg 4-4, Bozeman, MT 59715, USA

E-mail: William.Kunkel@bridgerphotonics.com; Mike.Thorpe@bridgerphotonics.com

Contents

S1. Transformation to single-scan equivalent distribution

To demonstrate the transformation from a persistence adjusted distribution to a single-scan equivalent distribution, consider the Cusworth cumulative emission rate distribution in the forms shown in Fig. S7. The first trace (blue squares) is the persistence adjusted distribution plotted at q, the second trace (green circles) is the same but remapped to $\bar{q}$, and the red trace (red dots) is the single-scan equivalent, which shows the cumulative sum with weighting by persistence g. The traces correspond to the different versions of the PDF plotted in Fig. 2, where the cumulative emission rate function has been computed using the discrete sums

$$a(x) = \frac{1}{\sum q} \cdot \begin{cases} \sum\limits_{q \geq x} q & \text{(persistence adjusted)} \\ \sum\limits_{\bar{q} \geq x} q & \text{(persistence removed)} \\ \sum\limits_{\bar{q} \geq x} g\bar{q} & \text{(single-scan equivalent)} \end{cases}, \tag{S1}$$

where q and $\bar{q}$ signify corresponding measurements of each source as defined by Eq. 1. The total emission rate (rightmost point on the curve) is smaller in the single-scan equivalent trace because the modified persistence g is always smaller than the observed persistence f. The distribution is not strongly reshaped by the persistence weighting. This can be seen from the similarity of the persistence-removed trace to the renormalized single-scan equivalent. The renormalized trace (dotted red line) is simply the single-scan equivalent curve vertically stretched to the height of the other two totals.

S2. Model fitting for 150 m aggregated emission sources

Results from the fit optimization are shown in Fig. S8. The CDF and residuals for each of the three comparisons mentioned in the main text are plotted along with the best fit. Fit parameters are shown in the upper left plot. GML residuals show that the sample CDF crosses the model multiple times without a bias toward the positive or negative direction. The Cusworth residuals show that larger emitters are somewhat overrepresented in comparison to the model, which could be a result of sample variation in the GML data set.

The expected number of observed sources in the comparison range for a sample of equal size to GML is $N_{\mathrm{GML}}(x \geq x_L)/h$. Fig. S8 shows $h = 0.89$ and $N_{\mathrm{GML}}(x \geq x_L) = 16$, which would predict 18.0 sources observed by a GML-sized sample in the comparison range. GML sample variation in the fat tail does not translate proportionally to uncertainty in the model function since support for the model fit comes predominantly from regions with large N, i.e. $x \geq 600$ kg h^{-1} for Cusworth and $x \geq 10$ kg h^{-1} for GML.

The p-value for the "GML to Cusworth" comparison changes somewhat with scaling by h. The scaled CDF and p-value in the rightmost plots of Fig. S8 can be compared to the "before scaling" version in Fig. 4. With scaling by h, the p-value increases from 0.831 to 0.943.

The overall scale factor between the Cusworth and GML distributions may be calculated by combining h with the ratio of number of detections expected in a hypothetical single scan over both distributions, controlling for the number of sources in each distribution. This is given simply by $N_{\mathrm{Cusworth}}(x \geq x_L)/N_{\mathrm{GML}}(x \geq x_L) \cdot h$, which is 15.6 using the numeric values in Fig. S8.

S3. Exclusion of pipelines from Cusworth data set

Inclusion of O&G pipeline sources in the Cusworth data set produces a negligible change in the CDF. By comparison, the effect of filtering the data to single emitter sources changes

the distribution significantly. Fig. S9 shows the CDFs for "with pipeline" and "without pipeline" data sets for 150 m and single emitter aggregation styles. Based on the moderately high p-values for the inclusion or exclusion of pipelines within each aggregation style, no statistically significant differences between the distributions are seen. However, the p-value for a comparison across aggregation styles is vanishingly small, meaning that the sample distributions differ substantially.

Despite the lack of significant change in the Cusworth distribution with the inclusion or exclusion of pipelines, small differences around the detection roll-off (300 $\mathrm{kg\,h^{-1}}$) lead to slightly different estimates of the detection sensitivity. PDFs for the two aggregation styles, with and without pipelines, are shown in Fig. S10. Comparing the model bounds at 95% confidence to respective cubic polynomial roll-off fits yields detection sensitivity intervals of 283-323 (with pipelines) and 290-328 $\mathrm{kg\,h^{-1}}$ (no pipelines) for 150 m sources, and 267-324 and 297-369 $\mathrm{kg\,h^{-1}}$, respectively, for single emitter sources. Since these intervals overlap significantly, the detection sensitivity roll-off can be considered as only weakly dependent on both types of data filter.

Figures

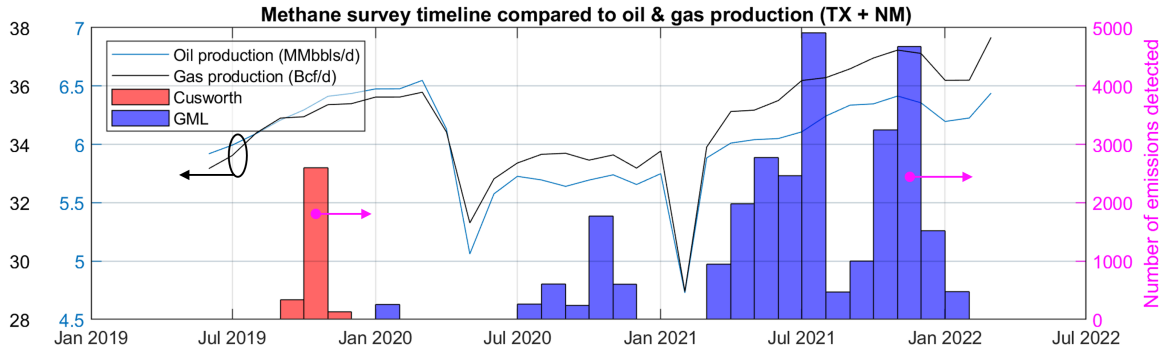

Figure S1: Oil and gas production[1] in Texas and New Mexico at the time of Cusworth and GML surveys.

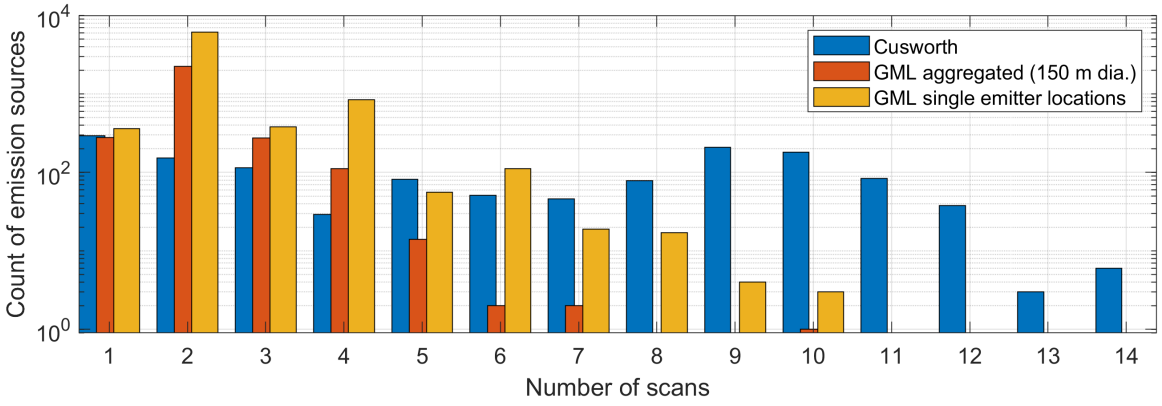

Figure S2: Histogram counting emission sources by number of scan repetitions.

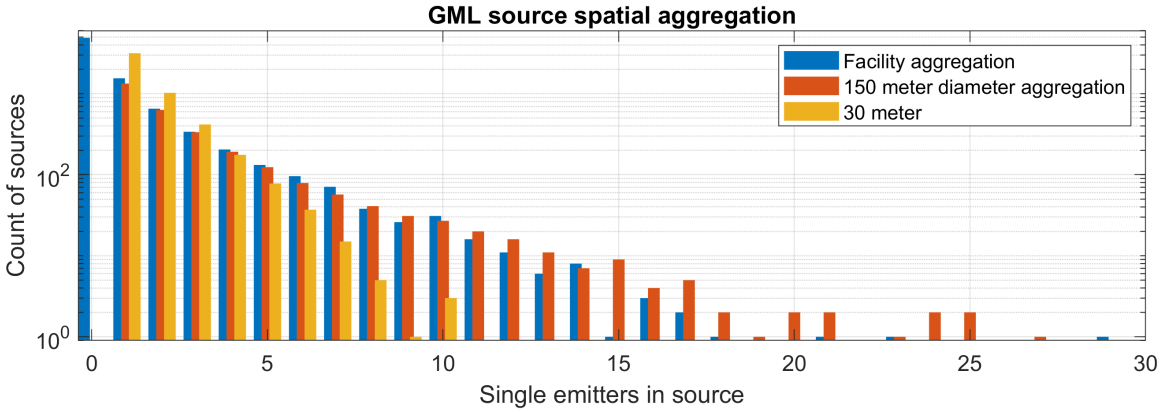

Figure S3: Histogram counting spatially aggregated sources by number of emitters in aggregation area.

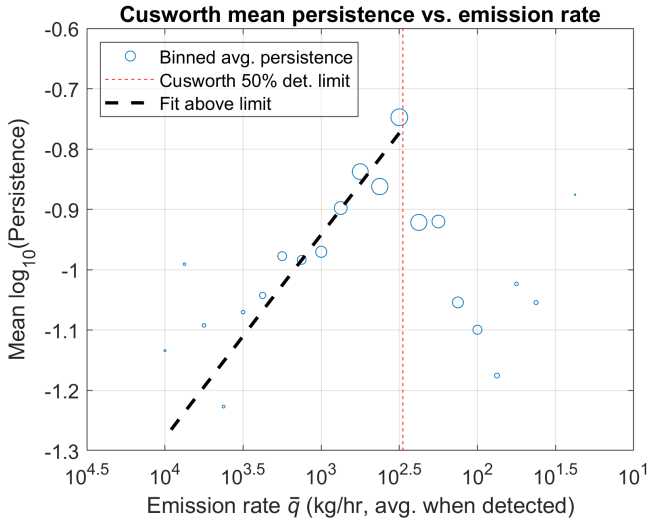

Figure S4: Cusworth modified persistence g plotted as a function of emission rate. Linear trend above the full detection limit breaks suddenly below the 50% detection limit. Marker area (circles) is proportional to number of emission sources in each bin.

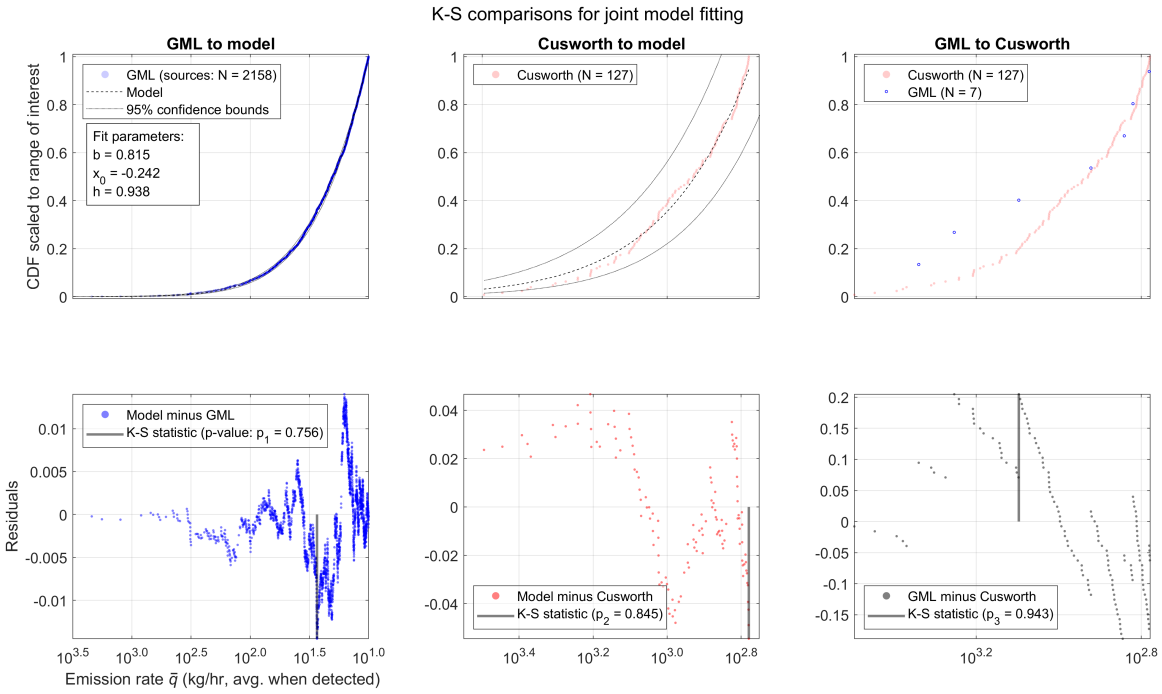

Figure S5: Joint model fitting of single emitter sources showing comparisons of cumulative distribution functions (CDF) and residuals.

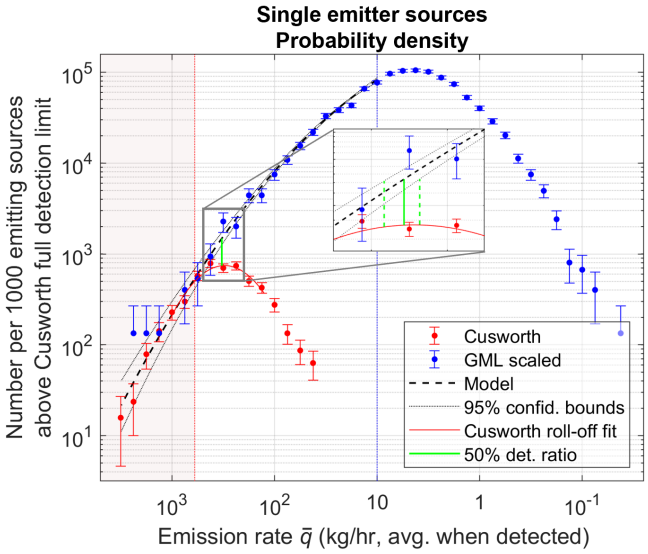

Figure S6: Scaled probability density functions of single-location emission sources. Zoomed in view near the Cusworth sensitivity limit (inset) shows the 50% detection ratio with respect to model function and its confidence bounds.

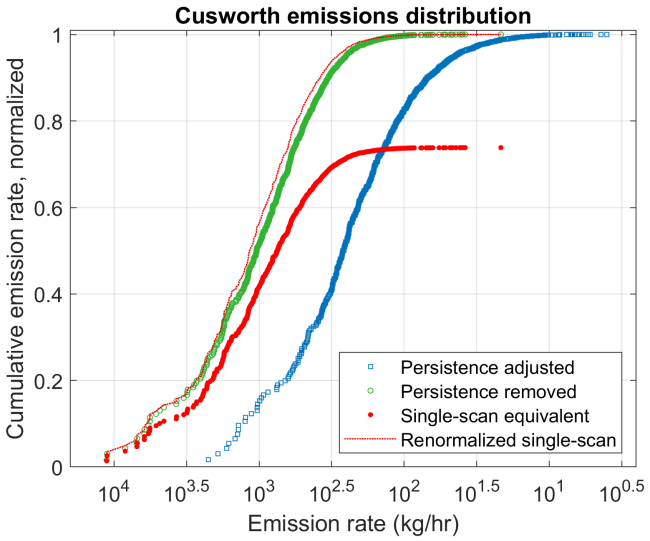

Figure S7: Cusworth cumulative emission rate distribution resulting from the different persistence treatments illustrated in Fig. 2.

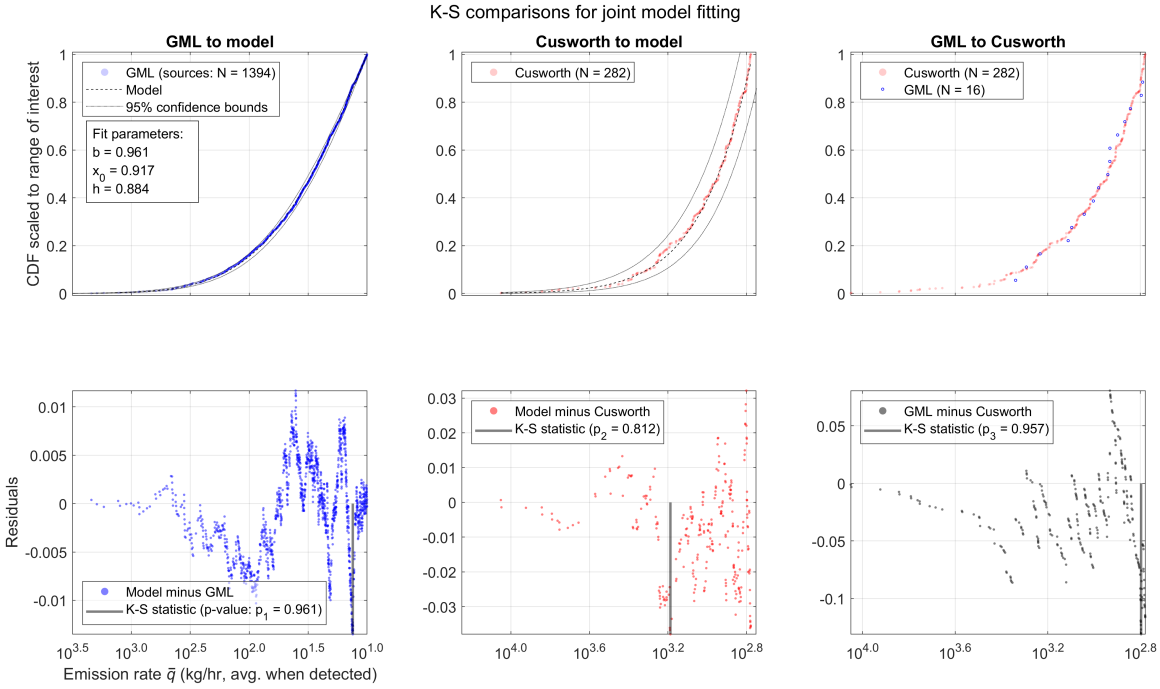

Figure S8: Joint model fitting of 150 m aggregated emission sources showing comparisons of cumulative distribution functions (CDF) and residuals.

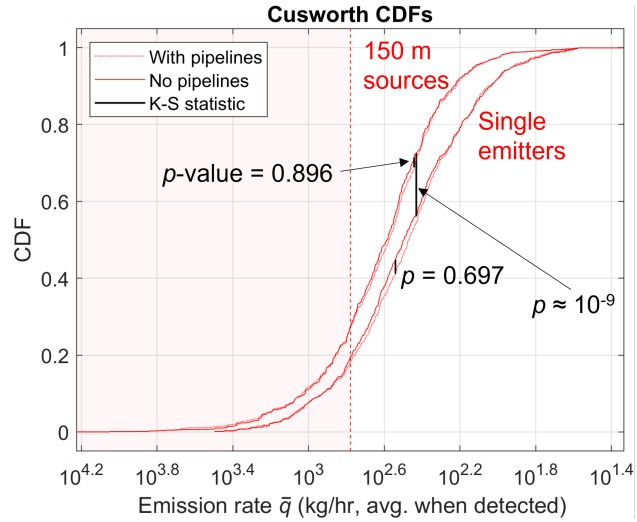

Figure S9: Comparison of Cusworth cumulative distribution functions (CDFs) over the whole range of emission rates in the sample. Data are filtered to include or exclude O&G pipeline emission sources at 150 m aggregation or single emitter sources. p-values are indicated for "with pipeline" and "without pipeline" comparisons within each source type and a "no pipeline" comparison across the two source types.

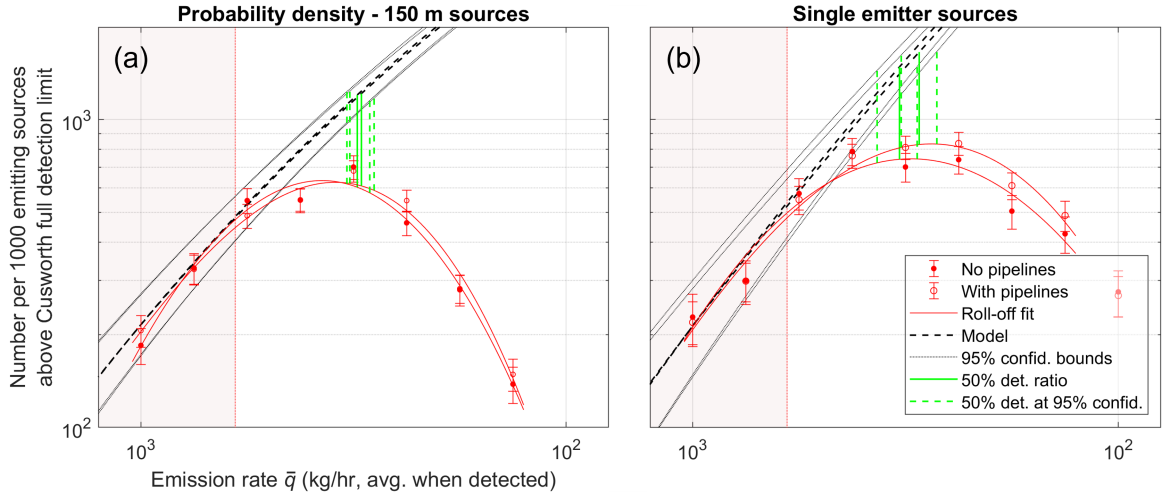

Figure S10: Cusworth probability density plots showing influence of O&G pipeline sources on emission distribution around detection roll-off. 150 m aggregated sources (a) and single emitter sources (b).

References

(1) U.S. Energy Information Administration, Monthly Crude Oil and Natural Gas Production (EIA-914). 2022; [Data set]. https://www.eia.gov/petroleum/production/#oil-tab (Retrieved 2022-Jun-30); see TX, NM "EIA Final mbbls/d" and "EIA Final MMcf/d".